

The Effect of Solute Suppressed Nucleation Effect and Latent Heat on the Grain Refinement of Cast Aluminum Alloy



LI JUN, JIANG HAITAO, WU XIAOYAN, LIU WENQIANG, and LU HONGZHOU

Grain refinement is the key to developing high-quality cast aluminum alloys. Based on the solute conservation theory and dendritic growth kinetics model, this paper developed a cellular automaton (CA) numerical model and fully considered the complex evolutionary processes, such as nucleation particle characteristics, nucleation-growth process, dynamic solute diffusion, and latent heat release during the solidification process of aluminum alloys. The CA model was used to quantify the role of solidification latent heat and solute diffusion in the grain nucleation process. The influence of solute suppressed nucleation (SSN) and solidification latent heat on the grain refinement effect of aluminum alloys are systematically studied. The results showed that when only considering the SSN effect, with the increase of nucleation density, the refinement efficiency decreases from 81.2 to 45.98 pct, and the decrease gradually decreases. This was mainly due to the increase of number of particles in the solute diffusion layer. The grain separation distance (GSD) became smaller than the size of the invisible nucleus region, reducing in the nucleation efficiency of the particles there. When the model further considered the effect of latent heat, the refinement efficiency was sharply dropped to 7 pct. The re-glow phenomenon caused by latent heat release limited the possibility of nucleation of small-sized particles and particles located in the SSN zone. Therefore, latent heat was found to be the main factor restricting grain refinement.

<https://doi.org/10.1007/s11663-024-03166-3>

© The Minerals, Metals & Materials Society and ASM International 2024

I. INTRODUCTION

AS the most widely used and mature aluminum alloy refiner in industry, the grain refining potency of Al-Ti-B refiner is less than 1 pct.^[1] For the aluminum with high Si content (> 5 wt pct), the refining potency of traditional Al-5Ti-1B refiners is poor. The two nucleation particles (NbAl_3 , NbTi_2) of Al-Nb-B refiner in aluminum melt and α -Al exhibited lower lattice mismatch and good wettability.^[2] What's more, it has been proved that Al-Nb-B refiner has ability to resist Si poisoning

and possesses better thermodynamic stability.^[3] Therefore, Al-Nb-B refiner showed better refinement effects in high Si aluminum alloys.^[4] Our previous studies have shown that Al-Nb-B grain refiner has a good refining effect in forged alloys with low Si content.^[5] However, the refining effect will gradually decrease with the increase of the addition amount. Therefore, it is necessary to study the further reasons restricting grain refinement.

The essence of restricting the further improvement of grain refinement degree is the reduction of refinement efficiency. In addition to the small lattice mismatch (< 10 pct)^[6] between the nucleated particles and the α -Al matrix, the refining efficiency of the inoculation is also related to the size of the inoculation particles^[1] and constitutional undercooling around particles.^[7] A growth restriction factor, named Q to quantify the effect of solute elements and content on dendrite growth inhibition was first proposed by Maxwell *et al.*^[8] They believed that Q mainly inhibited the release of latent heat, delayed the occurrence of recalescence, and provided more undercooling required for nucleation. Based on this, Greer *et al.*^[1] proposed a model to describe the nucleation size and free growth undercooling degree, believing that the critical nucleation undercooling degree is negatively correlated with the size of the

LI JUN is with the National Engineering Research Center for Advanced Rolling and Intelligent Manufacturing, University of Science and Technology Beijing, Beijing 100083, P.R. China and also with the NIO Automotive Technology (Anhui) Co., Ltd, Hefei, Anhui 230601, P.R. China. JIANG HAITAO, WU XIAOYAN, LIU WENQIANG are with the National Engineering Research Center for Advanced Rolling and Intelligent Manufacturing, University of Science and Technology Beijing. Contact e-mail: jianght@ustb.edu.cn LU HONGZHOU is with the CITIC Metal Co., Ltd., Beijing 100004, P.R. China.

Manuscript submitted October 29, 2023; accepted June 3, 2024.

nucleation substrate, *i.e.*, large-sized particles are usually easier to nucleate than small-sized particles. In 2011, Shu *et al.*^[9] proposed the solute suppressed nucleation (SSN) effect, stating that nucleated particles in the solute diffusion layer at the initial stage of nucleation will be suppressed due to compositional supercooling. However, there is a sufficient region of compositional supercooling outside the region of solute-rich layer, which will provide the supercooling and growth space required for heterogeneous nucleation of nucleated particles. Subsequently, St. John *et al.*^[10] proposed a similar concept of nucleation-free zone (NFZ) and developed a semi-quantitative model for predicting grain size-interdependence theory. The results showed that controlling the size of the NFZ was directly proportional to $1/Q$, and that an increase in Q increased the compositional supercooling required for nucleation. Finally the size of the SSN region was decreased. The research conclusion was later confirmed in the *in-situ* synchrotron radiation experiment of Xu *et al.*^[7]

From the above studies, it can be found that the latent heat of solidification and SSN effect (or NFZ) are the constraints to further refinement effect of the refiners. In the above studies, the nucleation and growth processes were usually described using analytical models developed. These analytical models based on the uniformly distributed grains, a relatively fixed range of SSN regions, and a uniform solute distribution. Therefore, these analytical models cannot reproduce the stochastic nature of grain nucleation locations and the complex interactions between nucleation and solute diffusion. It also cannot reveal the transient change processes of nucleation and solute diffusion. The SSN effect and latent heat of solidification were qualitatively investigated in the analytical models. This was related with the grain size was determined by the latent heat of solidification in gravity casting and the SSN effect in direct current casting.^[11]

Cellular automata (CA) model can quantitatively reveal the dynamic evolution process, isolate the physical mechanisms, and provide guidance for experiments. It is a powerful tool for studying the evolution of solidified microstructures. In this paper, a CA numerical model was established based on solute conservation law and dendrite growth kinetics model. The characteristics of nucleation particles, nucleation-growth process, dynamic solute diffusion, and the complex evolution of latent heat release were fully considered. Therefore, the role of solidification latent heat and solute diffusion in the process of grain nucleation was investigated qualitatively. The grain refinement effect and mechanism of Al-Nb-B in Al-Si-Mg-Cu with low Si contents will be clarified.

II. MODELING

The present model is based on three key assumptions:

- (1) The simulation model of multi-element alloys involves relatively complex parameters. It is currently a common practice to simplify it into a binary alloy

for simulating dendrite growth. As shown in Figure 1, the growth rates of Al-1.0Si, Al-0.8Mg, and Al-0.7Cu binary alloy dendrite tips under different undercooling degrees were calculated based on the LGK model as shown in Reference 12. From the figure, it can be seen that the limiting effect of Si element as a solute element in Al is stronger than that of other elements, and its content is higher. Therefore, Al-1.0Si binary alloy is used to approximate the solidification process of Al-1.0Si-0.8Mg-0.7Cu alloy.

- (2) The effect of melt convection on dendrite growth and solute diffusion was negligible.
- (3) The thermal diffusivity of Al-Si alloy is three orders of magnitude higher than that of the solute in the liquid phase. It is believed that the kinetics of dendrite growth are controlled by solute transport, and the temperature field in the calculation area is uniformly distributed.

A. Nucleation Model

The free growth model^[1] was used to depict the effect of nucleation particles on grain refinement. The critical nucleation undercooling on the particle was negatively correlated with the size of the particle in this model. The specific expression was as follows.

$$\Delta T_{fg} = \frac{4\sigma}{\Delta S_v d}, \quad [1]$$

where σ , ΔS_v , and d represented the solid-liquid interfacial energy, entropy of fusion per unit volume of Al, and nucleation particle diameter, respectively.

The relationship between the diameter and density of nucleated particles was statistically calculated according to microstructure and followed the logarithmic Normal Distribution function showed in Eq. [2].^[13]

$$\frac{dN_d}{dd} = \frac{N_0}{\sigma_d d \sqrt{2\pi}} \exp\left(-\frac{[\ln(d) - \ln(d_0)]^2}{2\sigma_d^2}\right), \quad [2]$$

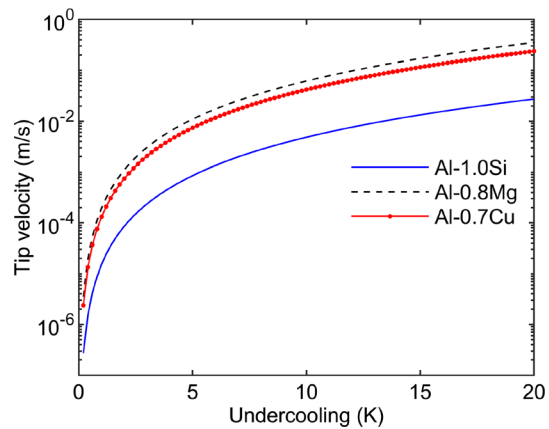


Fig. 1—Growth rates of binary alloy dendrite tips for Al-1.0Si, Al-0.8Mg, and Al-0.7Cu aluminum alloy under different undercooling.

where d and d_0 were the diameter and the geometric mean diameter of the particle or agglomeration, respectively. σ_d and N_0 were the geometric standard deviation and the total number of particles or agglomerations, respectively.

According to the statistical results of the Nb-containing phase in the backscatter scan image of the Al-Nb-B refiner microstructure, the fitting parameters were $d_0 = 1\mu\text{m}$, $d = 0.876\mu\text{m}$, $N_0 = 5.68 \times 10^{11}\text{m}^{-3}$ based on References 2,14.

B. Temperature Field and Concentration Field

The temperature field in the calculation domain was uniformly distributed and cooled at a certain cooling rate, calculated as^[15]:

$$\frac{\partial T}{\partial t} = -\dot{T} + \frac{L}{c_p} \cdot \frac{\partial f_s}{\partial t}, \quad [3]$$

where \dot{T} , L , c_p , f_s , represented cooling rate, latent heat released by solidification, specific heat capacity, and solid phase fraction, respectively.

In this model, the governing equation for solute diffusion was given by Fick's second law.^[16]

$$\frac{\partial C_L}{\partial t} = \frac{\partial}{\partial x} \left(D_L \frac{\partial C_L}{\partial x} \right) + \frac{\partial}{\partial y} \left(D_L \frac{\partial C_L}{\partial y} \right) + C_L(1-k) \frac{\partial f_s}{\partial t} \quad [4]$$

$$\frac{\partial C_s}{\partial t} = D_s \left(\frac{\partial^2 C_s}{\partial x^2} + \frac{\partial^2 C_s}{\partial y^2} \right), \quad [5]$$

where C_L and D_L represented the solute concentration and diffusion coefficient in the liquid phase, respectively. C_s and D_s represented the solute concentration and diffusion coefficient in the solid phase, respectively. k and f_s represented the partition coefficient and solid fraction, respectively.

C. Dendritic Growth Kinetics

The cell growth kinetics used the calculation method of dendritic growth kinetics based on interface solute equilibrium^[17]:

$$C_L^* = C_0 + \frac{T^* - T_0}{m_L} + \frac{\Gamma K f(\varphi, \theta_0)}{m_L} \quad [6]$$

$$\Delta f_s = (C_L^* - C_L) / (C_L^*(1 - k_0)), \quad [7]$$

where C_L^* was the interface equilibrium liquid solute concentration. T^* was the interface temperature. T_0 was the liquidus temperature at the initial concentration C_0 . m_L was the slope of the liquidus. K was the curvature of the solid-liquid interface, Γ was the Gibbs-Thomson coefficient. $f(\varphi, \theta)$ was a function of

the correlation between the anisotropy coefficients of the interface. φ was the angle between the interface normal and the x-axis. θ was the anisotropy function described the angle between the preferred growth direction of dendrites and the x-axis as follows.^[18]

$$f(\varphi, \theta) = 1 - \delta \cos[4(\varphi - \theta)], \quad [8]$$

where δ was the anisotropy coefficient. φ was calculated by the following formula^[19] and f_s represented the solid phase fraction of the unit:

$$\varphi = \arccos \left(\frac{\partial f_s / \partial x}{\sqrt{(\partial f_s / \partial x)^2 + (\partial f_s / \partial y)^2}} \right), \quad [9]$$

where K was the curvature of the solid-liquid interface unit which can be calculated by the variation of unit vector normal (VUVN) method^[19]:

$$K = \frac{\left[2 \frac{\partial f_s}{\partial x} \frac{\partial f_s}{\partial y} \frac{\partial^2 f_s}{\partial x \partial y} - \left(\frac{\partial f_s}{\partial x} \right)^2 \frac{\partial^2 f_s}{\partial y^2} - \frac{\partial^2 f_s}{\partial x^2} \left(\frac{\partial f_s}{\partial y} \right)^2 \right]}{\left[\left(\frac{\partial f_s}{\partial x} \right)^2 + \left(\frac{\partial f_s}{\partial y} \right)^2 \right]^{3/2}} \quad [10]$$

D. Numerical Implementation

To reduce the influence of grid anisotropy and simulate the dendrite orientation in any direction, the zigzag capture rule developed by Wei *et al.*^[19] was employed. The bilinear interpolation method was used to calculate the curvature of solid-liquid (SL) interface cells. The zigzag capture rule adopted a folded line capture method of alternating von Neumann neighbors and molar neighbors, which reduced the convenience of growth on the axis and diagonal directions. The bilinear interpolation method can disperse the sharp interface and improve the calculation accuracy of curvature by solving the weighted average of the solid phase scores of SL interface cells and neighboring and next-nearest neighbor cells. Therefore, the SL interface cell and neighboring cells fractions processed by bilinear interpolation were used in this paper for the calculation of the interface curvature, and the details of this method are described in Reference 20.

The numerical simulation calculation area was consisted of a 400×400 unit grid, with the grid unit side length was set to $2\mu\text{m}$. The nucleation points were randomly set according to the nucleation density in the calculation area. The cooling rate was set to 3.5Ks^{-1} with reference to the traditional Al-Si alloy gravity casting.^[21,22] In addition, the calculation area was uniformly set to periodic boundary conditions. The numerical simulation was completed on the programming software MATLAB R2022b based on the explicit algorithm. The thermophysical parameters of the Al-1.0 Si alloy used are shown in Table I.

Table I. Thermophysical Parameters Required for Dendritic Nucleation-Growth

Physical Properties	Value	References
Si Contents, C_0	1.0 pct	—
partition Coefficient, k	0.11	21
liquidus Slope, m	- 6.6K wt pct	21
Liquid Phase Diffusion Coefficient, D_L	$2.4 \times 10^{-9} \text{m}^2\text{s}^{-1}$	JMatPro
solid Phase Diffusion Coefficient, D_S	$1.5 \times 10^{-13} \text{m}^2\text{s}^{-1}$	JMatPro
Gibbs-Thomson Coefficient, Γ	$2.4 \times 10^{-9} \text{mK}$	21
Anisotropy Coefficient, δ	0.3	21
Latent Heat, L	$3.96 \times 10^5 \text{JKg}^{-1}$	23
Specific Heat Capacity, c_p	$880 \text{JK}^{-1}\text{Kg}^{-1}$	23
Solid-Liquid Interface Energy, σ	0.158Jm^{-2}	2
Melt Entropy Per Unit Volume, ΔS_V	$1.112 \times 10^6 \text{JK}^{-1}\text{m}^{-3}$	2

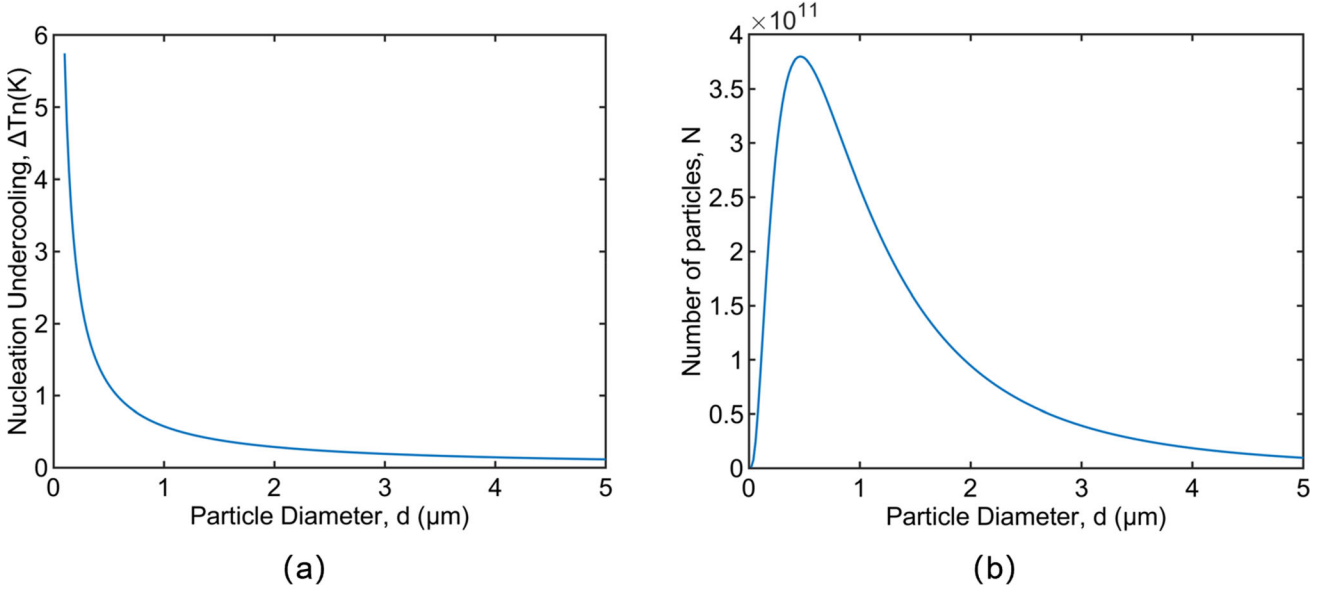


Fig. 2—(a) Nucleation size and undercooling distribution curve; (b) Logarithmic function curve of nucleation particle size and distribution density.

III. RESULTS AND DISCUSSION

A. Validation of Nucleation-Growth Model

The latest research by Li *et al.*^[3] on the refining mechanism of Al-Nb-B showed that the nucleation ability of NbB₂ phase was improved significantly due to the formation of NbAl₃ or metastable NbAl₃. The NbAl₃ phase distributed on the surface of NbB₂ reduced the mismatch between NbB₂ and α -Al reduced from 8.4 to 1 pct. Therefore, in this paper, both NbB₂ and NbAl₃ particles were considered as nucleation substrates.

Figure 2 shows the distribution density of NbAl₃ particle size and its relationship with the nucleation undercooling degree used for free growth in the nucleation model used in this paper. Figure 2(a) shows that the nucleation was at least 0.1 K at the larger part of the nucleation particle, which meant that during the nucleation process, a competitive nucleation process will be exited from large to small particle size. Figure 2(b) shows the fitted logarithmic normal distribution curve,

which was consistent with the results based on experimental statistics in Reference 14. Most particles with a particle size of 1 μm provided nucleation undercooling of 0.6K, and the proportion of large-sized particles that can provide smaller nucleation undercooling degree was low.

Figure 3 shows a comparison of the steady-state growth rate of dendrite tips predicted by the CA model and the analytical solution of LGK^[12] with a dendrite orientation of 0 deg. The detailed calculation of LGK was reported in previous research.^[20] The results in Figure 3 indicated that a good agreement was obtained at the undercooling degree of $\Delta T = 6\text{K}$. However, when $\Delta T > 6\text{K}$, the growth rate simulated by CA was lower than that of the LGK and the results were opposite at $\Delta T < 6\text{K}$. This was related with the analytical solution considering the three-dimensional geometric shape of dendrites. The geometric shape of the CA model was limited by the two-dimensional mesh shape and size. In addition, the discretization error that may

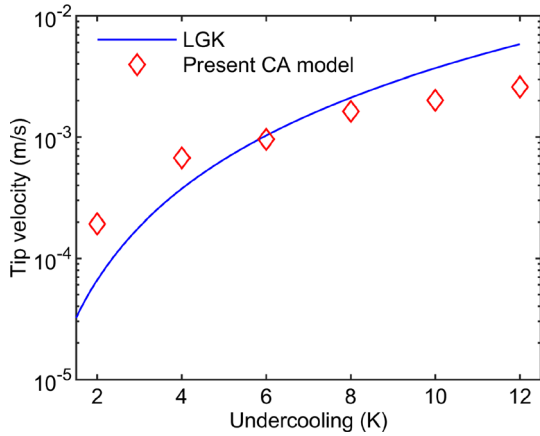


Fig. 3—Comparison of tip steady-state growth rate predicted by CA model and LGK.

be caused by modeling solute transport and solidification at the same length and time scale may also be the reason for the loss of accuracy at faster solidification rates. This simulation results were consistent with the predictions of Wang,^[24] Rolchigo^[25] and Gu *et al.*^[22].

B. The Effect of SSN on Grain Refinement

Figure 4 shows the equiaxed crystal morphology and concentration field distribution of different nucleation particle densities at 2.9297s considering only the SSN effect without solidification latent heat. It can be seen that the grain size was decreased significantly with the increase of nucleation density linearly. The secondary dendrite arm disappeared gradually.

It can be obtained from Figure 4(a) that when the nucleation density N_0 was $5.68 \times 10^{11} \text{m}^{-3}$, the dendrites exhibited random dendrite orientation and developed secondary and tertiary dendrite arms. It was found that these developed dendrite arms usually appeared in spaces without the dual effects of solute diffusion and other dendrite physical obstacles, and filled these spaces with continuous growth. Then the entire solidification process was completed. In addition, the liquid phase ratio of the red part in Figure 4(a) was significantly higher than that in Figure 4(b) through (d). This indicated that the speed of dendrites was significantly slower than the latter three. The relationship between dendrite growth rate, secondary dendrite arms, and solutes can be explained by constitutional supercooling (CS) theory: As solidification progresses, excess solutes were enriched at the SL interface and discharged into the entire melt through diffusion. Therefore, in the later stage of solidification, the degree of solute enrichment at the SL interface and the average solute concentration in the remaining liquid phase were increased simultaneously. According to CS theory, higher liquid solute concentration suggested lower liquid phase line temperature. In other words, a negative temperature layer appeared at the front of the SL interface, leading to interface instability and higher-order dendrites. On the

other hand, higher liquid solute suggested greater undercooling required for solidification. Undercooling was the only driving force for dendrite growth.^[16] Therefore, the growth rate of dendrites was decreased with the increase of solute content.

Furthermore, as shown in Figures 4(b) through (d), with the increase of nucleation density and the decrease of secondary dendrite arm, the continuous equiaxed crystal nucleation filled the remaining space at a faster growth rate than solute diffusion. This seriously weakened the possibility of higher-order dendrite growth and thereby achieved the effect of grain refinement.

Figure 5 shows the change curves of grain size and nucleation efficiency as the nucleation density linearly increased in Figure 4. The refining potency E was expressed as $E = N_g/N_0$. N_0 represented the nucleation density. N_g represented the effective nucleation density obtained after counting the number of equiaxed crystals. The relationship between N_g and l (grain size) was expressed^[26] in Eq. [11].

$$l = \left(\frac{0.5}{N_g} \right)^{1/3} \quad [11]$$

It can be seen from Figure 6, that when considering the SSN effect, the nucleation efficiency and grain size both decreased exponentially with the increase of nucleation density. The nucleation efficiency gradually decreased from 81.2 to 45.98 pct, and the grain size decreased from 180 to 40 μm . Fan *et al.*^[26] also obtained a similar conclusion when the grain separation distance (GSD) was greater than the length of the intangible nucleation zone, including nucleation particles x_{NFZ} , *i.e.*, $\text{GSD} > x_{\text{NFZ}}$. The SSN effect had limited influence on nucleation. With the increase of nucleation density, the number of particles distributed inside the solute diffusion layer. At this time, $\text{GSD} < x_{\text{NFZ}}$, where the nucleation probability of particles was very small. The nucleation efficiency further was decreased.

In order to further analyze the reasons for the decrease of nucleation efficiency and grain size, the dynamic change process of the liquid phase CS in Figure 5(a) was extracted as shown in Figure 6. The research work^[16] showed that the CS was shown in Eq. [12], where $T_{i,j}(t)$ represented the actual temperature of the liquid phase, and T^{eq} represented the liquid phase temperature at the initial component C_0 .

$$\Delta T = T^{eq} + m_L(C_L - C_0) - T_{i,j}(t) \quad [12]$$

The white dashed line represented the equiaxed crystals generated relative to the previous iteration step in Figure 6. It can be seen that as the solidification process progressed, the CS in the entire calculation domain gradually increased. The undercooling layer on the periphery of the equiaxed grains changed from isotropic to a quadruple symmetrical morphology that grew along the crystallographic direction. The CS at the undercooling layer was always lower than that at the melt far from the SL interface. Comparing Figures 6(b) and (c), it can be found that the CS required for nucleation in the latter was greater than that in the

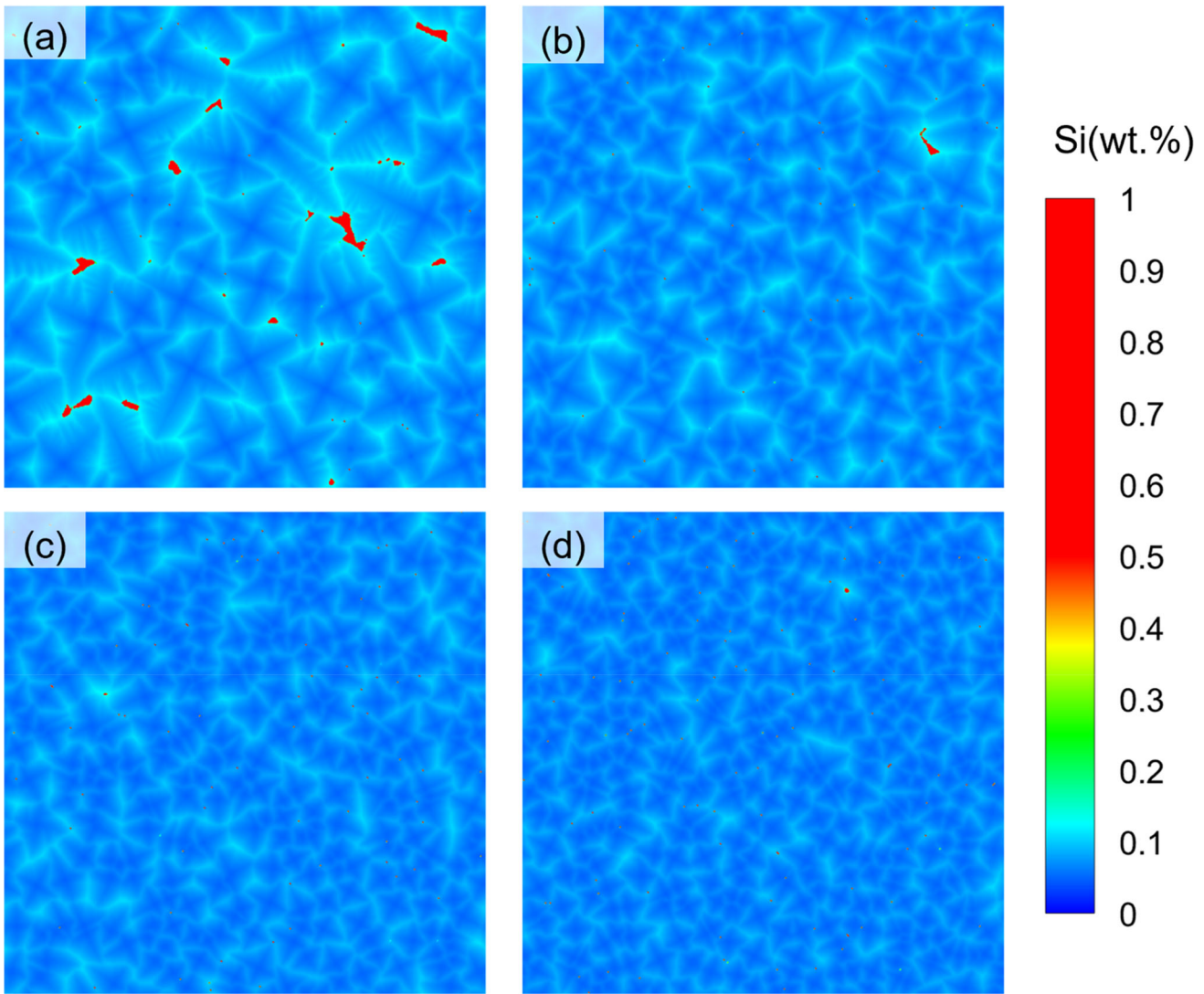


Fig. 4—The concentration field distribution of Al-1.0Si (wt pct) alloy during solidification under different nucleation densities: (a) $5.68 \times 10^{11} \text{m}^{-3}$, (b) $3 \times 5.68 \times 10^{11} \text{m}^{-3}$, (c) $6 \times 5.68 \times 10^{11} \text{m}^{-3}$, (d) $9 \times 5.68 \times 10^{11} \text{m}^{-3}$.

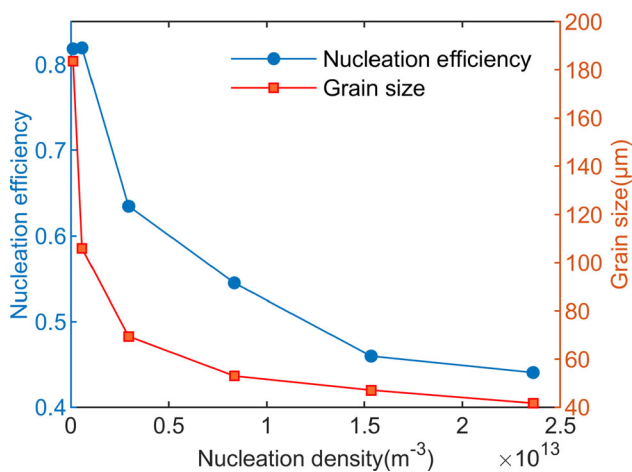


Fig. 5—The variation of nucleation efficiency and grain size with nucleation density.

former. There may be two reasons for this phenomenon. On the one hand, the particle size at this location was smaller, and its own nucleation CS was larger. On the other hand, the newly formed nucleation particles in Figure 6(c) were located at the undercooling layer of the pre-nucleation grains. Due to the SSN effect, the CS at this location was lower than that in the calculation domain far from the SL interface, and further undercooling was required to stimulate nucleation.

Figure 7 shows the distribution of undercooling along the A-A line at two times in Figures 6(c) and (d). It can be seen that the undercooling at the two larger grains decreased continuously with the superposition of the continuous SSN caused by growth. Therefore, suppressed effect of SSN effect increased sharply with the decrease of GSD. This was consistent with the conclusion of Prasad *et al.*^[27] in studying the competition effect between solute accumulation rate and cooling rate on

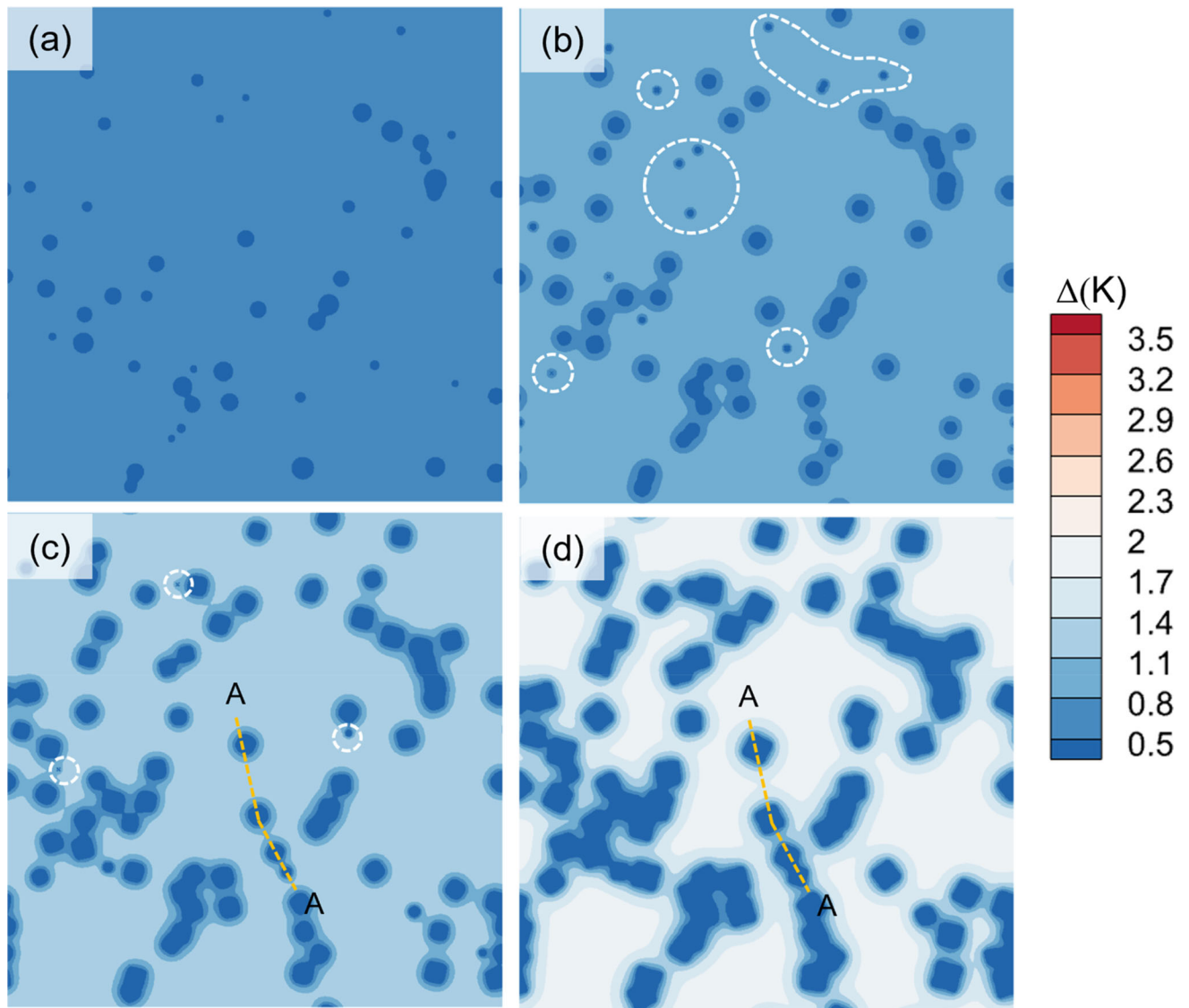


Fig. 6—Evolution of component undercooling with the solidification process: (a) 0.1302s, (b) 0.2604s, (c) 0.3906s, (d) 0.5208s.

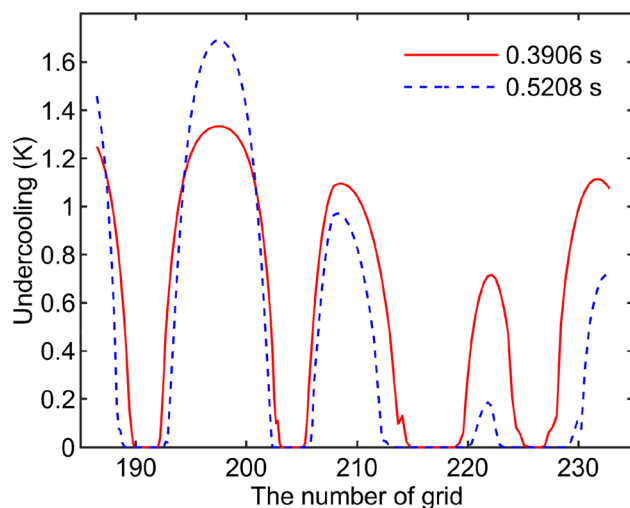


Fig. 7—Distribution of undercooling along line A-A.

nucleation. It was found that even at higher cooling rates, the accumulation rate of solutes in the later stage of growth will be the main factor affecting nucleation.

As was shown in Figure 8, the evolution curve of the number of nucleations and the temperature at the monitoring point in the middle of the calculation domain in Figure 6 was statistically analyzed. The number of excitation nucleations increased exponentially with the increase of undercooling. The nucleation model with logarithmic normal distribution of nucleation density and size used in this article was also consistent with the trend of cumulative nucleation grain quantity observed by Xu *et al.*^[7] in X-ray *in-situ* synchrotron radiation. Since the influence of solidification latent heat was not considered, the cooling rate decreased linearly with time. Corresponding to Figure 6(d), the number of nucleations increased slightly after 0.5s. This was mainly because in the larger GSD area, the further increased in cooling increases the

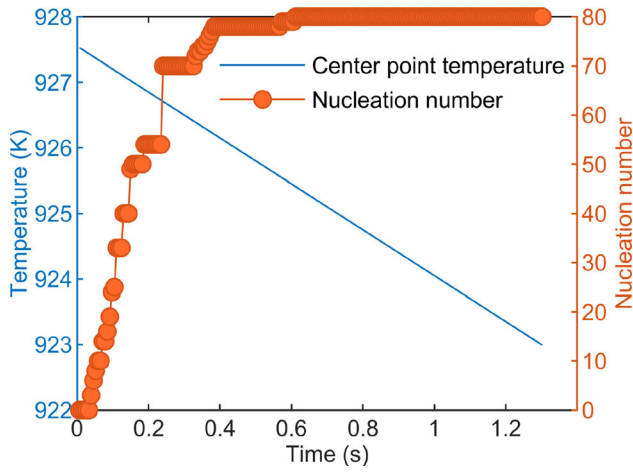


Fig. 8—The number of nucleations and the temperature at the monitoring point in the middle of the calculation domain in Figure 7.

nucleation probability of smaller particles affected by the SSN effect. This was similar to the white dashed line area in Figure 6(c).

C. The Effect of Latent Heat on Grain Refinement

Figures 9(a) through (c) show the microstructure of Al-1.0Si-0.8Mg-0.7Cu alloy with the addition of 0.03 wt pct, 0.06 wt pct, and 0.09 wt pct Nb elements, respectively. The details of the experiment were provided in previous research.^[5] Figures 9(d) through (f) show the grain distribution with a linear increase in nucleation density under the combined effect of solidification latent heat and SSN, with a cooling rate of 3.5Ks^{-1} . In the experiment, the area method was used to measure the surface grain density N_s according to Eq. [13]^[11]:

$$N_s = \frac{N_1 + 0.5N_2 + 1}{A}, \quad [13]$$

where N_1 was the number of complete grains in region A , and N_2 was the number of grains on the edge of region A .

For the convenience of comparison, only the number of nucleation was counted here. The number of microstructure nucleation in the experiment was 42, 50, and 62, while the simulation results were 36, 55, and 66. It can be seen that the experimental and simulation

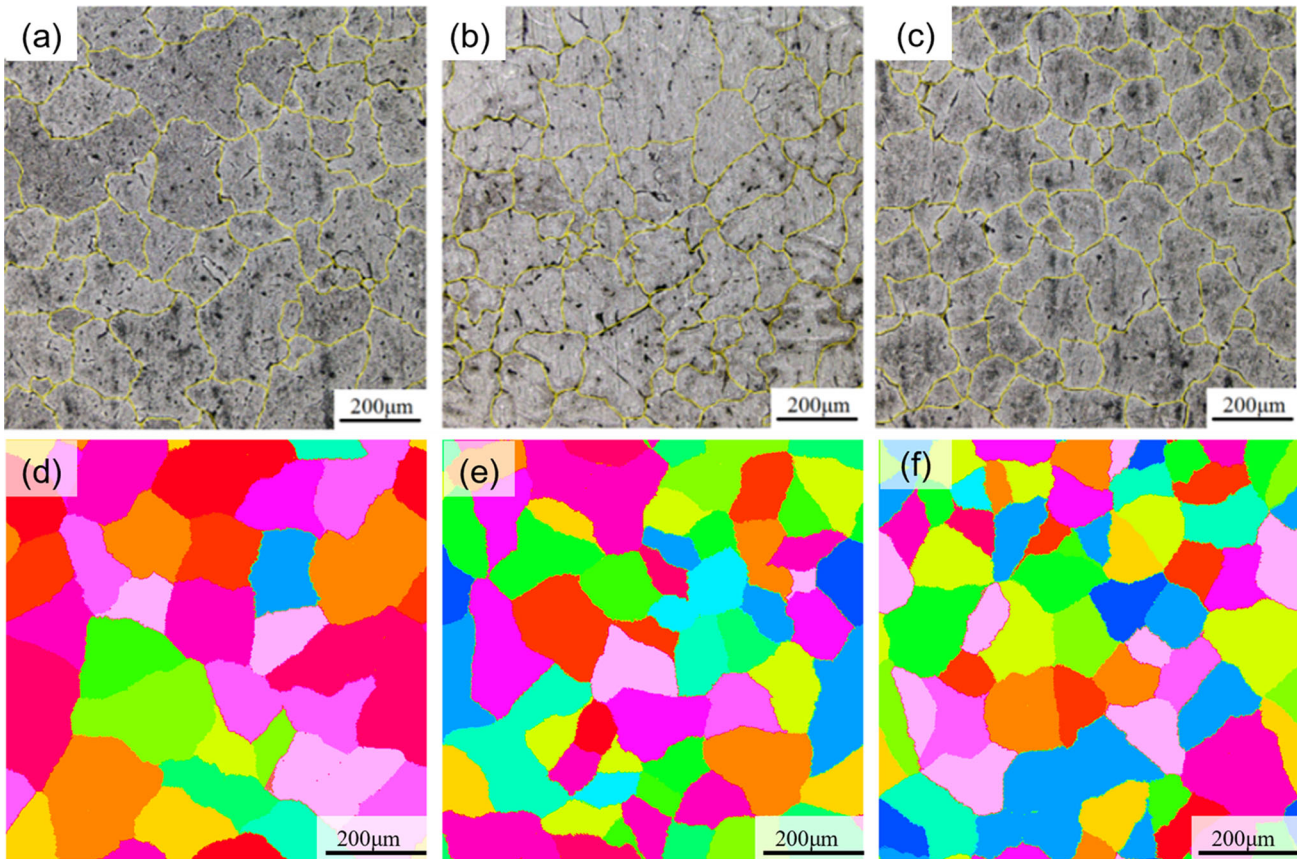


Fig. 9—Comparison of experimental results with different Nb addition amounts and numerical simulations considering solidification latent heat and SSN effect modes: (a) 0.03(wt pct)Nb, (b) 0.06(wt pct)Nb, (c) 0.09(wt pct)Nb, (d) $5.68 \times 10^{11}\text{m}^{-3}$, (e) $3 \times 5.68 \times 10^{11}\text{m}^{-3}$, (f) $6 \times 5.68 \times 10^{11}\text{m}^{-3}$.

results showed good quantitative consistency when considering the solidification latent heat. It was worth noting that the simulated grains were slightly larger with the increase of nucleation density. This was because of the influence of different amounts of refiners on the size of nucleation particles in the melt. In addition, the degradation of the refining effect caused by the adsorption agglomeration and gravity settling behavior of nucleation particles in the melt were ignored.^[2,13]

By comparing Figures 4 and 9, the grain size decreased significantly after considering the effect of solidification latent heat. In order to further quantify the combined effect of the SSN and solidification latent heat on grain refinement, the evolution of grain size and refining potency under different nucleation densities was statistically analyzed. As shown in Figure 10(a), without considering the SSN effect, the refining potency was 100 pct when $N_g = N_0$. It can be seen that as the nucleation density increased, the effect and trend of SSN and solidification latent heat on grain size were similar to those under complete nucleation without considering the SSN. The downward trend gradually decreases. At the maximum nucleation density, the grain size increased from 47.11 μm considering only the SSN effect to 116.72 μm when considering the combined effect. That was to say that the release of latent heat was the main factor of grain size, which was similar to the research of Du *et al.*^[11] using the extended KWN analytical model. However, Du *et al.* completely ignored the influence of SSN effect and adopted a uniformly distributed nucleation spacing to reduce the influence of superimposed diffusion fields. It was believed that the SSN effect in the early stage of nucleation was not significant in their research.

Figure 10(b) shows the effect of the SSN and solidification on the refining potency. After considering the solidification latent heat, the refining potency dropped sharply from 81.2 pct at the lowest nucleation density ($1.09 \times 10^{11} \text{m}^{-3}$) to 50 pct. As the nucleation

density increased to $2.95 \times 10^{11} \text{m}^{-3}$, the refining potency further decreased to 13 pct, and slowly decreases to 7 pct as the nucleation density continues to increase. At this time, the refining potency considering only the SSN effect was 45.98 pct. Therefore, further analysis of the effect of latent heat on grains was needed.

Taking Figure 9(e) as an example, the evolution of nucleation number and temperature over time during the solidification process was statistically analyzed, as shown in Figure 11. The trend of nucleation quantity change was similar to that in Figure 8, which only considered the SSN effect. The difference was that the nucleation process only terminated in 0.05 s, while the nucleation time was extended to 0.65s when only considering the SSN effect. As shown by the black dashed line in the figure, the termination point of the nucleation coincided with the recalescence point of the temperature monitoring curve at the center of the computational domain. At this point, the cooling rate was equal to the release rate of latent heat, which cannot provide more nucleation undercooling for nucleation particles. Therefore, nucleation events similar to that in Figure 6(c) will not occur. At the same time, the release of latent heat greatly reduced the undercooling in the computational domain and inhibited the growth of dendrites. This was mainly due to the lower undercooling during the initial solidification stage. The slower increase in solid fraction, the smaller latent heat release. The undercooling was increased subsequently, and the growth rate of dendrites accelerated, making the latent heat release more significant. At this time, the released latent heat was greater than the heat carried away by cooling, leading to a temperature rise and the occurrence of recalescence phenomenon.^[28]

From the relationship between the nucleation size and the undercooling of free growth model shown in Figure 2(b), it can be seen that the nucleation sequence sequentially went from large-sized particles to small-sized particles. Then recalescence phenomenon occurs

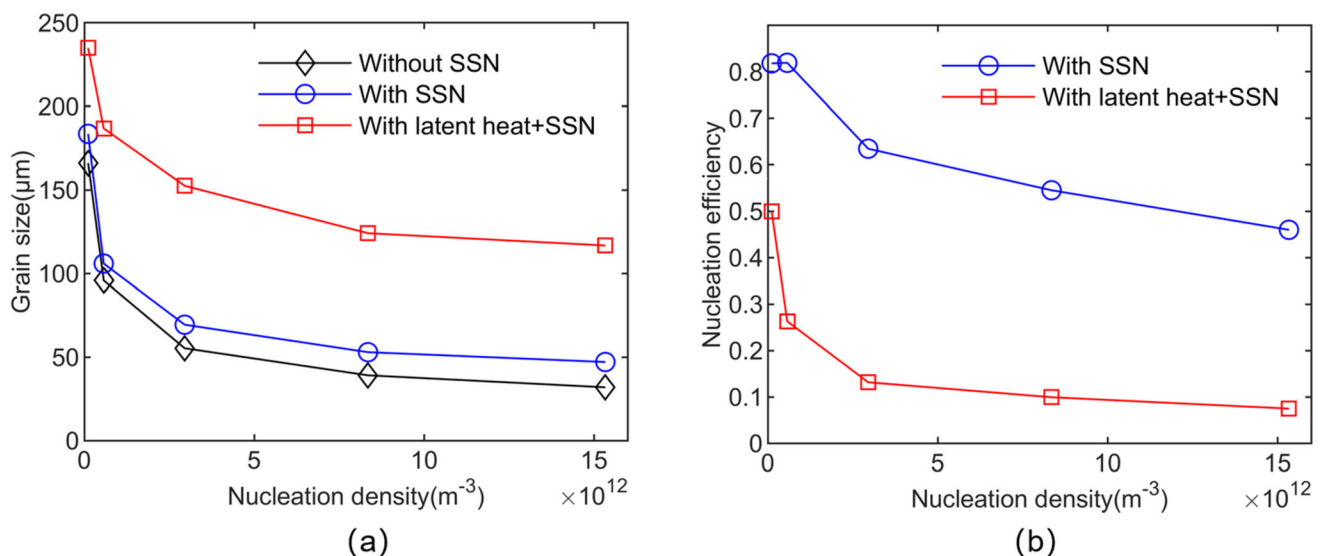


Fig. 10—Comparison of grain size: (a) refining potency (b) considering the SSN effect and solidification latent heat.

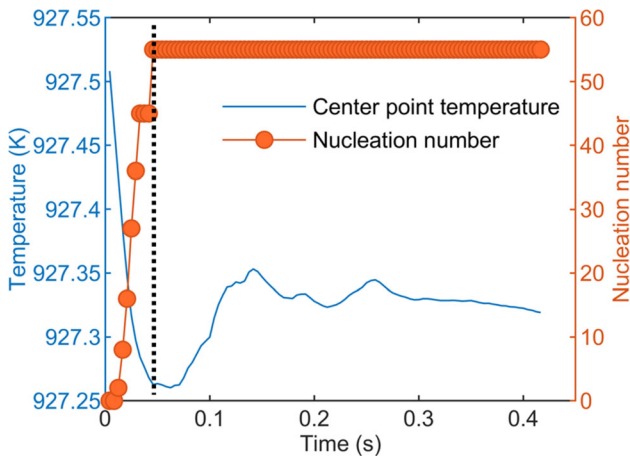


Fig. 11—The variation of nucleation quantity and temperature curve over time.

until the last smaller particle nucleates. The remaining small particles or particles located in the SSN region will not participate in nucleation. In other words, in order to further refine the grain size, it was necessary to have a sufficient number of larger particles before the recalescence. As shown in Figure 2(a), the proportion of larger particles was very small, which suggested that an increase in nucleation density can cause a small number of particle excitation nucleation, resulting in a lower refining potency.

The minimum refining potency in this article was 7 pct, which was significantly different from the 1 pct refining potency reported in the Reference [1]. This was because the establishment process of CA model did not consider these conditions, including the viscous force, van der Waals force, buoyancy between particles and the melt, and gravity of the particles themselves. The interaction of these forces will lead to particle aggregation and sedimentation, reducing refining potency. At the same time, this article also overlook the effects of coarsening, collision, convection, and stirring on the particle size distribution of particles/aggregates, which may lead to the hard impact of grown grains on particles and prevent nucleation.^[1]

The analysis of SSN and solidification latent heat showed that the dispersed grain separation spacing and reheating time were key factors in determining nucleation. Many methods for improving grain refinement efficiency can be proposed correspondingly, such as reducing the lattice compatibility between particles and collective elements, dispersing particle distribution, optimizing particle size, prolonging recalescence time, and increasing the maximum nucleation undercooling during recalescence.

IV. CONCLUSIONS

This paper established a nucleation model that considers the logarithmic normal distribution of nucleation particle size density. Based on the solute conservation CA model for dendrite growth, the effects of

solute diffusion and solidification latent heat release on grain refinement are studied. The following conclusions can be drawn from the results obtained:

- (1) The increase of nucleation density can refine the grains. This was related with the continuous nucleation and growth of equiaxed crystals filling the remaining space at a faster growth rate than solute diffusion. Thus the concentration of solute at the solid-liquid interface and the average liquid solute concentration in the melt was reduced. Finally, the interface became instability and the growth of higher-order dendrites was inhibited.
- (2) When only considering the SSN effect, the refining potency decreases from 81.2 pct to 45.98 pct with the increase of the nucleation density. This was attributed to the gradual increase of particles inside the solute diffusion layer, causing GSD to be smaller than x_{NFZ} , reducing the nucleation efficiency of particles at this location.
- (3) The release of solidification latent heat is the main factor affecting grain refinement. When considering the SSN effect and solidification latent heat, the minimum refining potency is only 7 pct. The occurrence of the recalescence phenomenon limits the possibility of nucleation of smaller particles and particles located in the SSN region. The increase in nucleation density can only lead to the nucleation of larger particles with a smaller proportion, reducing the overall refining potency.

CONFLICT OF INTEREST

The authors declare no conflict of interest.

REFERENCES

1. A.L. Greer, A.M. Bunn, A. Tronche, P.V. Evans, and D.J. Bristow: *Acta Mater.*, 2000, vol. 48, pp. 2823–35.
2. X. Jin, R. Li, and Q. Li: *Metall. Mater. Trans. A*, 2021, vol. 52, pp. 1077–94.
3. Y. Li, Y. Jiang, B. Liu, Q. Luo, H. Bin, and Q. Li: *J. Mater. Sci. Technol.*, 2021, vol. 65, pp. 190–201.
4. W. Xiaoyan, Z. Huarui, J. Feng, Y. Ying, J. Lina, and H. Zhang: *Rare Metal Mater. Eng.*, 2018, vol. 47, pp. 2017–22.
5. L. Jun, J. Haitao, and W. Xiaoyan: *Mater. Res. Express*, 2023, vol. 10, 086513.
6. Z. Fan: *Metall. Mater. Trans. A*, 2013, vol. 44, pp. 1409–18.
7. X. Yijiang, C. Daniele, D. Qiang, H.M. Ragnvald, A. Lars, and L. Yanjun: *Acta Mater.*, 2017, vol. 140, pp. 224–39.
8. I. Maxwell and A. Hellawell: *Acta Metall.*, 1975, vol. 23, pp. 229–37.
9. D. Stjohn, M. Qian, M. Easton, et al.: *Acta Mater.*, 2011, vol. 59(12), pp. 4907–21.
10. X. Yijiang, C. Daniele, H.M. Ragnvald, and L. Yanjun: *Acta Mater.*, 2018, vol. 149, pp. 312–25.
11. D. Qiang and Y. Li: *Acta Mater.*, 2014, vol. 71, pp. 380–89.
12. J. Lipton, M.E. Glicksman, and W. Kurz: *Mater. Sci. Eng.*, 1984, vol. 65, pp. 57–63.
13. Z. Fan, F. Gao, Y. Wang, H. Men, and L. Zhou: *Prog. Mater. Sci.*, 2022, vol. 123, 100809.
14. X. Jin, Y. Li, K. Ma, F. Yanan, E. Guo, Z. Chen, G. Qinfen, Y. Han, T. Wang, and Q. Li: *Scr. Mater.*, 2020, vol. 187, pp. 142–47.

15. M. Zhu, S. Pan, D. Sun, and H. Zhao: *ISIJ Int.*, 2010, vol. 50, pp. 1851–58.
16. W.L. Wang, W.Q. Liu, X. Yang, R.R. Xu, and Q.Y. Dai: *J. Mater. Sci. Technol.*, 2022, vol. 119, pp. 11–24.
17. M.F. Zhu and D.M. Stefanescu: *Acta Mater.*, 2007, vol. 55, pp. 1741–55.
18. B. Maïke, W. Mareike, D. Jörg, and K. Florian: *Metall. Mater. Trans. A*, 2023, vol. 2023, pp. 1–5.
19. L. Wei, Y. Cao, X. Lin, M. Wang, and W. Huang: *Comput. Mater. Sci.*, 2019, vol. 156, pp. 157–66.
20. W. Wang, W. Liu, X. Yang, X. Rongrong, and Q. Dai: *Modell. Simul. Mater. Sci. Eng.*, 2021, vol. 30, 015005.
21. R. Chen, X. Qingyan, and B. Liu: *Comput. Mater. Sci.*, 2015, vol. 105, pp. 90–100.
22. G. Cheng, D.R. Colin, and A.L. Alan: *Metall. Mater. Trans. B*, 2019, vol. 50, pp. 123–35.
23. X. Ao, H. Xia, J. Liu, and Q. He: *Mater. Des.*, 2020, vol. 185, 108230.
24. W. Wang, S. Yin, S. Luo, and M. Zhu: *Metall. Mater. Trans. B*, 2019, vol. 50, pp. 1531–41.
25. M.R. Rolchigo and R. LeSar: *Comput. Mater. Sci.*, 2018, vol. 150, pp. 535–45.
26. G. Feng and F. Zhongyun: *Metall. Mater. Trans. A*, 2022, vol. 2022, pp. 1–3.
27. A. Prasad, L. Yuan, P.D. Lee, and D.H. St John: *Acta Mater.*, 2013, vol. 61, pp. 5914–27.
28. W. Weiling, Y. Shiwei, and L. Sen: *Metall. Mater. Trans. B Process Metall. Mater. Process. Sci.*, 2019, vol. 50, p. 1531.

Publisher's Note Springer Nature remains neutral with regard to jurisdictional claims in published maps and institutional affiliations.

Springer Nature or its licensor (e.g. a society or other partner) holds exclusive rights to this article under a publishing agreement with the author(s) or other rightsholder(s); author self-archiving of the accepted manuscript version of this article is solely governed by the terms of such publishing agreement and applicable law.